nature COMMUNICATIONS

ARTICLE

Received 8 May 2015 | Accepted 3 Jul 2015 | Published 13 Aug 2015

DOI: 10.1038/ncomms8993 OPEN

Visualizing nanoscale excitonic relaxation properties of disordered edges and grain boundaries in monolayer molybdenum disulfide

Wei Bao[1,2,3,*], Nicholas J. Borys[1,2,*], Changhyun Ko[3], Joonki Suh[3], Wen Fan[3], Andrew Thron[1,2], Yingjie Zhang[2,4], Alexander Buyanin[2,5], Jie Zhang[1], Stefano Cabrini[1,2], Paul D. Ashby[1,2], Alexander Weber-Bargioni[1,2], Sefaattin Tongay[3,6], Shaul Aloni[1,2], D. Frank Ogletree[1,2], Junqiao Wu[2,3], Miquel B. Salmeron[2,3] & P. James Schuck[1,2]

Two-dimensional monolayer transition metal dichalcogenide semiconductors are ideal building blocks for atomically thin, flexible optoelectronic and catalytic devices. Although challenging for two-dimensional systems, sub-diffraction optical microscopy provides a nanoscale material understanding that is vital for optimizing their optoelectronic properties. Here we use the 'Campanile' nano-optical probe to spectroscopically image exciton recombination within monolayer MoS_2 with sub-wavelength resolution (60 nm), at the length scale relevant to many critical optoelectronic processes. Synthetic monolayer MoS_2 is found to be composed of two distinct optoelectronic regions: an interior, locally ordered but mesoscopically heterogeneous two-dimensional quantum well and an unexpected ~300-nm wide, energetically disordered edge region. Further, grain boundaries are imaged with sufficient resolution to quantify local exciton-quenching phenomena, and complimentary nano-Auger microscopy reveals that the optically defective grain boundary and edge regions are sulfur deficient. The nanoscale structure–property relationships established here are critical for the interpretation of edge- and boundary-related phenomena and the development of next-generation two-dimensional optoelectronic devices.

[1] Molecular Foundry, Lawrence Berkeley National Laboratory, 1 Cyclotron Road, Berkeley, California 94720, USA. [2] Materials Sciences Division, Lawrence Berkeley National Laboratory, 1 Cyclotron Road, Berkeley, California 94720, USA. [3] Department of Materials Science and Engineering, University of California Berkeley, 210 Hearst Mining Building, Berkeley, California 94720, USA. [4] Applied Science and Technology Graduate Program, University of California, 210 Hearst Mining Building, Berkeley, California 94720, USA. [5] Department of Chemistry, University of California Berkeley, 419 Latimer Hall, Berkeley, California 94720, USA. [6] Department of Materials Science and Engineering, Arizona State University, P.O. Box 876106, Tempe, Arizona 85287, USA. * These authors contributed equally to this work. Correspondence and requests for materials should be addressed to P.J.S. (email: pjschuck@lbl.gov).

The emergence of two-dimensional (2D) monolayer transition metal dichalcogenides (ML-TMDC) as direct bandgap semiconductors[1,2] has rapidly accelerated the advancement of room temperature, 2D optoelectronic devices[3–10]. However, performance of the active ML-TMDC materials often falls far below theoretical expectations, particularly for critical factors such as carrier mobility and quantum yield[4,11]. Overcoming such macroscopic limitations in lower-dimensional systems requires a nanoscale understanding of the materials. Central to 2D optoelectronic applications, light-matter interactions in ML-TMDCs are dominated by a manifold of tightly bound exciton states[12–14] with remarkably strong absorption cross-sections[1] and appreciable photoluminescence (PL)[2]. Unlike traditional 2D quantum wells, the enhanced coulombic interaction between the electrons and holes in ML-TMDCs stabilizes the excitonic states at room temperature. The most prevalent states are the low-energy A exciton and the charged A− trion[15], and their relative populations can be tuned by electrostatically changing the electron density of the material[15]. Furthermore, adsorbates[16], strain[17,18] and piezoelectric[7] effects can reversibly modify the energy of these states, whereas structural discontinuities such as grain boundaries[19] (GBs) and defects[16] can enhance or quench luminescence.[19] While scanning tunnelling[20,21] and transmission electron[19,22,23] microscopies have probed atomic-scale electronic properties and structural defects in ML-TMDCs, optical investigations of these excited states have been diffraction limited and thus unable to directly resolve nanoscale excitonic phenomena. Near-field optical microscopy provides a route to explore material properties below the diffraction limit in 2D systems[24–27]. However, nanoscale optical visualization and spectroscopy of inelastic light-matter interactions (such as nano-PL) in two dimensions constitutes a formidable challenge, necessitating a non-traditional approach that confines optical excitation and collection without hindering spectral analysis.

Here we utilize the previously established sub-diffraction hyperspectral imaging capability of the Campanile probe[28] to spectroscopically map nanoscale excited-state relaxation processes in chemical vapour deposition (CVD)-grown MoS_2 on length scales that are commensurate with characteristic optoelectronic properties (for example, the exciton diffusion length and defect separations). The enhanced resolution reveals significant nanoscale optoelectronic heterogeneity and enables the quantification of exciton-quenching phenomena at GBs. Further, in-depth analysis of the nanoscale spatial irregularities of the excited-state PL reveals a disordered edge region that is ~300-nm wide and has important implications for device engineering and edge-related phenomena.

Results

Nanoscale heterogeneity in the PL of ML-MoS_2. Compared with ML-TMDCs produced by exfoliation from bulk crystals, CVD-grown ML-TMDCs are appealing for device applications where high yield and large area production is required. Figure 1a illustrates hyperspectral near-field microscopy of CVD-grown ML-MoS_2 (see Supplementary Fig. 1 and Supplementary Note 1 for optical characterization and synthesis details). With the Campanile probe, optical excitation and collection are spatially confined to the nanogap at the apex of the tip, which is scanned over the sample, recording a full emission spectrum at each position[28] (see Supplementary Figs 2 and 3 and Supplementary Notes 2 and 3 for experimental and fabrication details). The spatial distribution of the integrated PL intensity (Fig. 1b) exhibits nanoscale fluctuations that are unresolved by conventional confocal optical microscopy of the same flake (Fig. 1c). Simultaneously collected topographic images indicate that these nanoscale variations are not topographical artefacts (Supplementary Fig. 4). Thus, significant nanoscale optoelectronic disorder is present in these materials.

Spectral analysis of the PL averaged over the extent of the flake reveals that the emission arises from the radiative recombination of the A exciton at ~1.84 eV and its A− trion at ~1.81 eV (ref. 15), which overlap strongly, as shown in Fig. 1d. The relative energies and populations of these two states intimately depend on numerous factors such as carrier and defect densities, screening, strain and band-bending effects[16–18]. Correspondingly, the nano-PL spectrum that is acquired at each point contains a wealth of information about the local optoelectronic properties. To robustly map spectral variations in the nano-PL, we characterize single-point emission spectra using the 'spectral median', which is defined as the emission energy that divides the PL into low- and high-energy regions of equal intensity (Fig. 1d). While the spectral median in itself fails to deconvolve energetic shifts from changes in the relative intensities of the states, it more reliably captures relative spectral changes in noisy data than numerical fitting.

A nano-PL map of another ML-MoS_2 flake is shown in Fig. 2. Spatial variations in the intensity (Fig. 2a) and emission energy (Fig. 2b) are observed across the flake in addition to a decrease in PL intensity near the edges. These trends are observed in all of the ML-MoS_2 flakes that were investigated in this study (Supplementary Fig. 5) and do not change over an order of magnitude of excitation power (Supplementary Fig. 6). In ML-MoS_2, increased relative emission of the trion is correlated with a reduction in the overall PL intensity[15]. To explore this type of behaviour in our spatially resolved data, we plot the integrated intensity of the PL acquired at each spatial position versus its emission energy (that is, its spectral median) in Fig. 2c. Two distinct clusters are observed. By systematically segregating the data points into either an internal interior region or a peripheral edge region (see Supplementary Fig. 7 for details), we find that the brighter cluster of correlated data points (orange data points) belongs to the interior of the ML-MoS_2, while the significantly more scattered, dimmer cluster of points (blue data points) belongs to an ~300-nm peripheral edge region. In the interior, the intensity and energy of the PL are correlated, with the higher-energy emission tending to be brightest. Such behaviour is consistent with increased emission intensity from regions with reduced trion populations. In contrast, the emission energy of the PL from the edge region is more disordered, spanning nearly the entire range of emission energies at the lower emission intensities.

As previously noted, shifts in the spectral median value can arise from changes in the relative amounts of exciton and trion emission and/or energetic shifts of the excitonic resonances. So, the correlation between the PL intensity and its spectral median alone cannot unambiguously unravel the underlying optoelectronic behaviour of the edge and interior regions. Thus, to further probe the behaviours observed in the correlation plot of Fig. 2c, the emission spectra are grouped by their total emission intensity into one of five equally spaced ranges spanning 1–6 kCts (ranges I, II, III, IV and V in Fig. 2c). For each intensity range, the emission spectra are summed, and the average spectrum is calculated as shown in Fig. 2d,e for the interior and edge regions, respectively (see Supplementary Fig. 8 for alternative intensity ranges). In this manner, the spectral characteristics of bright areas to those of dim areas can be compared with significantly improved signal-to-noise ratios over the single-pixel data. In the interior, we confirm that the primary spectral difference between bright and dim regions is the relative intensity of the low-energy emission from the trion state (Fig. 1d). Dim areas exhibit enhanced relative trion emission, indicating that the local

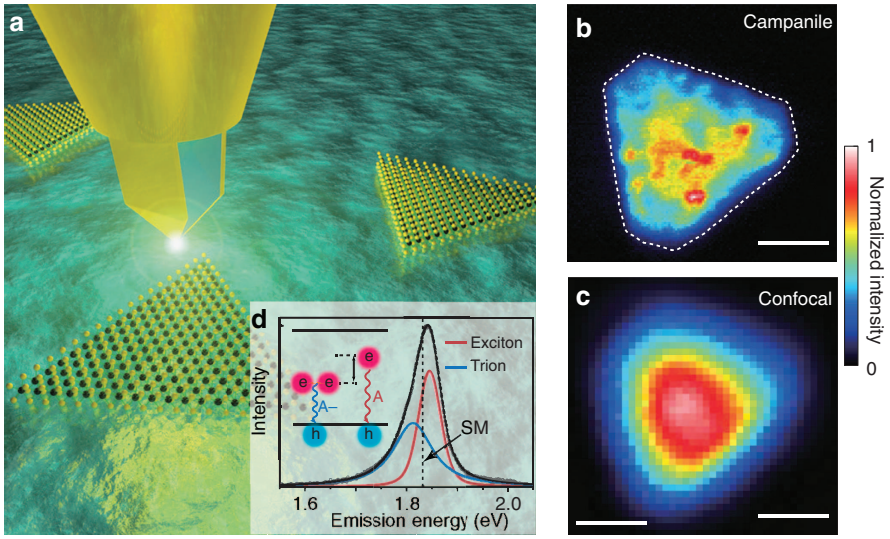

Figure 1 | Nano-optical imaging of PL in ML-MoS_2. (**a**) Illustration of near-field excitation and collection of the PL from ML-MoS_2 using the Campanile near-field probe where the optical laser excitation (2.33 eV) and collection of sample emission are confined to the apex of the tip[28] to produce high-resolution optical maps. At each pixel a full PL spectrum is acquired. (**b**) Map of the PL emission intensity of a triangular ML-MoS_2 flake using the Campanile probe. The white dashed line indicates the flake boundary as determined from the shear-force topography. Scale bar, 1 μm. (**c**) An image of the same flake acquired with scanning confocal microscopy using a ×100, 0.7-NA air objective. Scale bar, 1 μm. (**d**) Near-field nano-PL spectrum averaged over the spatial extent of the ML-MoS_2 flake. The emission contains two peaks arising from the radiative recombination from exciton (A) and trion (A −) states[15]. The dashed vertical line shows the position of the spectral median (SM) that splits the spectrum into equal amounts of high and low energy counts and is used to quantify spectral variations in the lower signal-to-noise spectra of individual spatial positions acquired during fast scans. All data were acquired under ambient conditions. NA, numerical aperture.

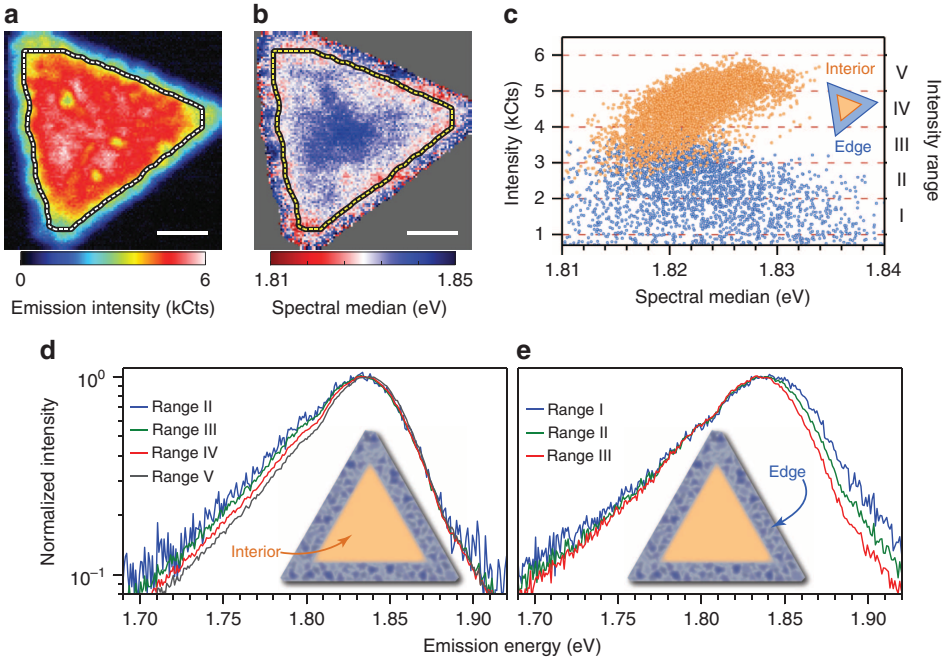

Figure 2 | Optoelectronic discrimination between edge and interior regions of ML-MoS_2. (**a**,**b**) Nano-PL images of emission intensity and SM (defined in Fig. 1d), respectively, of a single flake of ML-MoS_2. The dotted line marks the boundary between the interior of the flake and a ~300-nm wide periphery edge. Scale bars, 1 μm. (**c**) Emission intensity of each pixel plotted against its spectral median value for the interior (orange data points) and the edge regions (blue data points). Each data point in **c** corresponds to an emission spectrum recorded at a different position. The emission spectra from the interior and edges can be further grouped by their total emission intensity into one of five ranges (I, II, III, IV and V). (**d**) Averaged emission spectra of the interior data points for the intensity ranges II, III, IV and V (range I does not contain any interior data points) plotted on a normalized, semi-log scale for comparison. (**e**) Likewise, average emission spectra for the data points from the edge region for the intensity ranges I, II and III (ranges IV and V do not contain any data points from the edge region).

PL intensity inversely correlates with the population of trions. This behaviour likely arises from localized regions of increased carrier density that enhance the formation of trions and increase non-radiative Auger recombination, which reduces the local PL quantum yield[15].

Surprisingly, the PL of the edge region does not exhibit systematic variations in the relative intensity of the trion. Instead, PL emission from dimmer areas in the edge region (range I, Fig. 2e) is broadened to higher energies, indicating that the edge region is substantially more disordered than the interior. Further, emission from lower-energy states is apparently favoured in the edge region. Such a spectral signature implies the edge forms a 2D mosaic of localized, inhomogenously broadened emitters where excitations are funneled to low-energy sites similar to other mesoscopically disordered semiconductor systems such as organic conjugated polymers[29] and quantum-dot solids[30] (see Supplementary Note 4 for further discussion). It is clear that the edge region in synthetic MoS_2 is more complicated than just its atomic termination and a metallic edge state[20,21,31]. Because such disorder is foreseeably deleterious for carrier transport, it may also shed light on carrier mobility in MoS_2 where both hopping and band transport mechanisms have been reported[11]. Presumably, hopping mechanisms dominate in the disordered edge area as opposed to high mobility band transport in the interior. Future studies that combine nano-PL with scanning tunnelling microscopy (STM) or time-resolved spectroscopy will prove crucial in more precisely characterizing this critical edge region in ML-MoS_2.

To confirm the excitonic nature of the optoelectronic variations of the interior region seen in Fig. 2, the spatial interplay between excitons and trions is explicitly resolved in a smaller region ($0.5 \times 4\,\mu m$; Fig. 3a) of the same MoS_2 flake in Fig. 3. Single-point spectra were recorded with improved signal to noise using a longer integration time, enabling reliable fitting of the exciton and trion peaks (Fig. 3b). The emission intensity of each position is plotted against the corresponding ratio of the exciton and trion intensities in Fig. 3c and confirms that increased trion formation correlates with reduced PL quantum yield in the interior of the flake. Further, Fig. 3d shows the distribution of the exciton–trion splitting, indicating an average value of ~ 36 meV for this sample. The energetic splitting of the two states is directly related to the sum of the trion-binding energy and the Fermi energy in the system[15]. Although the splitting appears to be relatively uniform spatially, subtle variations could still possibly be uncovered with even higher resolution measurements in the future. Further, the spread of the values (~ 3 meV) is similar to that observed by changing the Fermi energy via electrostatic gating[15], envisaging studies that combine gating functionality with nano-PL characterization.

Excited-state quenching at grain boundaries. Whereas single-crystalline flakes of ML-MoS_2 can be anatomized into an interior and edge, disruptions to the crystalline structure can also occur during the CVD growth process. Isolated polycrystalline MoS_2 flakes can form intricate star-like structures while aggregates of

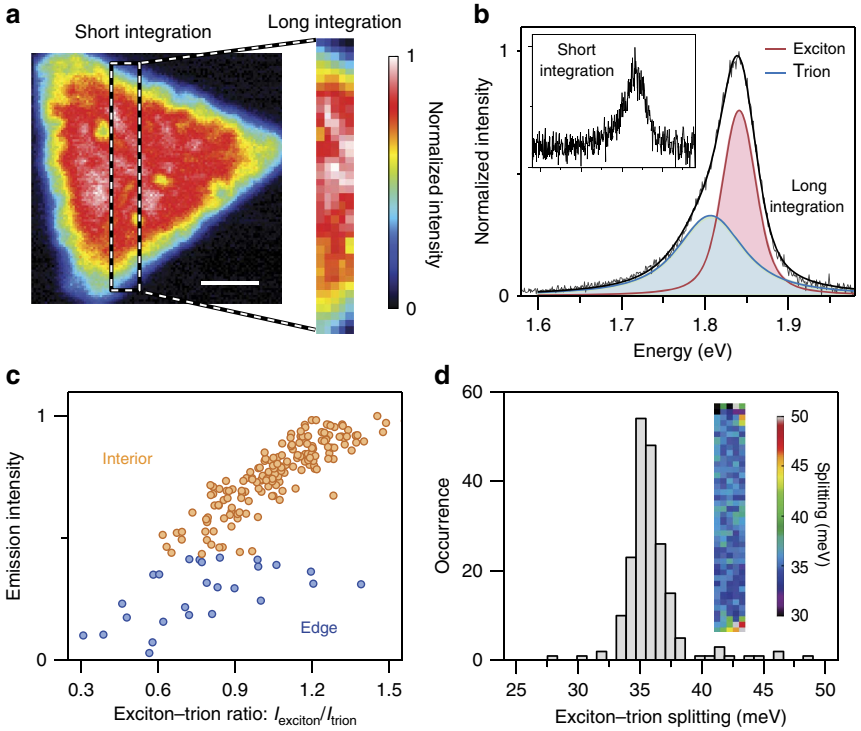

Figure 3 | Imaging spatial variations of the relative population and energetics of the A − trion. (**a**) A smaller region (dashed rectangular box) of the ML-MoS_2 flake from Fig. 2 is imaged with a longer pixel integration time (10 s) and reduced pixel density (100 nm per pixel) to increase the signal to noise of the near-field spectra. Scale bar, 1 μm. (**b**) Representative spectrum from a single pixel showing the improved signal-to-noise ratio of the 10 s pixel integration time of the slow scan compared with the 0.2 s pixel integration time of the fast scan (inset; covering the same spectral range as the main panel). The reduced noise of the slow scan enables fitting of the spectrum as a sum (black line) of peaks for the exciton state (A; red curve) and the trion state (A −; blue curve). The peak profiles are largely Lorentzian, but the best fits were achieved with a Voigt profile that convolves a pure Lorentzian with an underlying Gaussian distribution to account for inhomogeneous broadening effects. (**c**) PL emission intensity plotted against the exciton–trion ratio for each point in the interior (orange data points) and in the edge (blue data points) regions. (**d**) Statistical distribution and spatial distribution (inset) of the energetic separation between exciton and trion states.

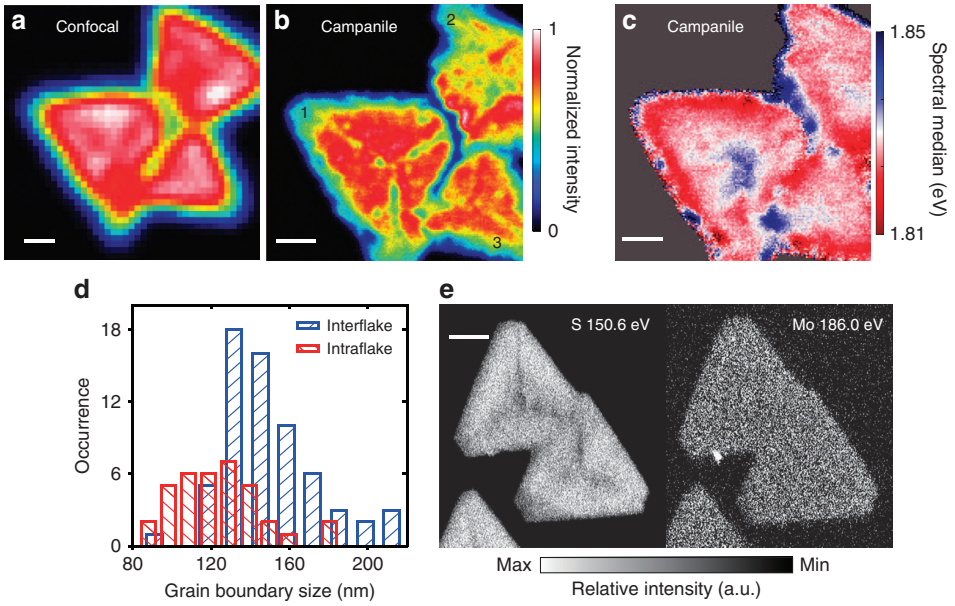

Figure 4 | Excited-state quenching of GBs and elemental mapping of ML-MoS_2. Far-field confocal micro-PL (**a**) and nano-PL (**b**) images of an aggregate of three flakes (labelled 1, 2 and 3) forming three interflake GBs. In the interior of flake 1, radial intraflake GBs are observed extending from the centre towards the apexes of the triangular flake. The interflake GB quenches the PL intensity by 50–80%, whereas the intraflake GB quenches the PL intensity by ~20%. Scale bars, 1 μm. (**c**) Map of the emission energy (that is, the spectral median value defined in Fig. 1d). Scale bar, 1 μm. (**d**) Histograms of the half width at half max sizes of the interflake and intraflake GBs, which are measured from the spatial extent of the PL reduction and sampled semi-equidistantly along the respective features (see Supplementary Fig. 9 for more details). (**e**) Nano-Auger elemental mapping of S and Mo on a similar multiflake aggregate from the same growth run. Both the edge region and GBs are S-deficient, while the Mo composition is uniform over the flakes. Scale bar, 2 μm.

flakes that merge during growth form complex polycrystalline patchworks[19,23]. The resulting GBs can significantly alter the local optoelectronic properties of the flake interior[19,32]. For example, some types of GBs are known to quench excitons, locally reducing the PL quantum yield[19], but the limited resolution of conventional optical microscopy fails to precisely resolve the quenching phenomena. In Fig. 4, confocal micro-PL (Fig. 4a) and Campanile nano-PL (Fig. 4b) maps of three MoS_2 flakes (labelled 1, 2 and 3) that merged during growth are compared. Although the confocal optical microscopy image (Fig. 4a) exhibits a mostly uniform PL intensity distribution within each flake, indicating a 'high-quality' sample, substantial nanoscale fluctuations are observed in the nano-PL image. Furthermore, a reduction in the PL intensity that corresponds to an exciton-quenching region marks the boundaries between flakes 1 and 2 as well as flakes 2 and 3. This effect is better resolved by the Campanile probe, more precisely quantifying the reduction in PL intensity. In addition to these interflake GBs, three narrow regions where the PL is quenched by ~20% extending radially from the centre of flake 1 (also in flake 3 and others shown in the Supplementary Fig. 5) are also better resolved in the nano-PL map. Interestingly, these GBs do not seem to alter the energetics of the PL, as can be observed in the nano-PL map of the emission energy in Fig. 4c, which is mostly devoid of systematic variations in the vicinity of the intra- and interflake GBs.

The structural width of a GB is on the order of the atomic-scale lattice spacing[19,23], but acting as a non-radiative recombination centre[19], its optoelectronic width (that is, the size of the quenching region) will be enlarged due to exciton diffusion (~24 nm (ref. 19)), which itself can be locally enhanced by band bending or carrier-depletion zones. In Fig. 4d, the extents of the exciton-quenching regions are statistically quantified by analysing multiple line cuts across inter- and intraflake GBs (see Supplementary Fig. 9 for details). The widths show substantial disorder, varying between 80–160 and 90–210 nm for the intra- and interflake GBs, respectively, and are not limited by our estimated resolution of ~60 nm (Supplementary Fig. 10 and Supplementary Note 5). Previous optical studies with limited resolution (~500 nm) proposed that the exciton quenching at GBs could not be accounted for by exciton diffusion alone, but fell short of directly quantifying the effect[19]. Here the mesoscopic extent of exciton quenching is confirmed and quantified with average sizes of 150 and 120 nm for the inter- and intraflake GBs, respectively. Interestingly, nano-Auger spectroscopy maps of ML-MoS_2 flakes from the same CVD growth run, shown in Fig. 4e (and Supplementary Fig. 11), reveal that the GBs and edge regions are S-deficient, consistent with previous results that show a 'Mo-rich' edge[22]. Such S-deficient regions in MoS_2 suggest probable *n*-doping near these boundaries[19] and also are suspected to have a higher density of mid-gap trap states[19,22], which may contribute to the local reduction in PL quantum yield.

Discussion

The results that are presented here bridge STM investigations of the electronic structure of ML-MoS_2 near GBs[32] and edges[20,21] to macroscopic optical imaging and spectroscopy measurements. In the vicinity of GBs, a complex reduction of the electronic bandgap over nanoscale distances is observed with STM[32], which may also influence the exciton-quenching effect. Further, earlier STM work on ML-MoS_2 has shown that an atomic metallic edge state is formed at the external boundary of the flakes[20,21]. Here we show that CVD-grown MoS_2 flakes are also enclosed by a larger disordered edge region that we hypothesize forms during the termination of the growth process (that is, the cooling step)[22]. Thus, the edge of synthetic ML-MoS_2 is more complex than just atomic-scale reconstructions of the crystalline interior—a crucial consideration that may help to explain observed edge-related phenomena such as resonantly enhanced second harmonic generation[31] and even enhanced catalytic activity[33]. Ultimately,

directly connecting these effects necessitates multimodal characterization using nano-PL techniques and STM on the same sample, which although challenging, is possible in principle and would be a very powerful study.

Altogether, our results provide a new insight into the rich optoelectronic properties of CVD-grown ML-MoS_2 by resolving exciton relaxation processes with sub-diffraction resolution. Significant nanoscale heterogeneity is observed, and distinct optoelectronic systems corresponding to a pristine interior, disordered edges as well as intra- and interflake GBs in synthetic ML-MoS_2 are revealed. Disorder induced by the growth process can produce a mesoscopic edge region that is more complex than just a reconstruction of the crystalline interior. This region must be considered when interpreting edge-related phenomena[31,33] and perhaps avoided when making edge-specific electrical contacts to ML-MoS_2 in optoelectronic devices[34]. Furthermore, the disordered edge region and GBs are expected to reduce device performance, especially carrier mobility and recombination efficiency. GBs are found to quench excitons over $\sim$150 nm, providing an initial quantitative basis to estimate their effects in 2D optoelectronic devices. Such detailed information on the subtle variations in optoelectronic properties and their relationship to corresponding nanometre scale structure within synthetic ML-TMDCs enhances the understanding of these materials, sets the stage for future multimodal nanoscale optoelectronic studies and will hopefully guide the future development of high-quality 2D materials and next-generation devices.

Methods

Sample growth. ML-MoS_2 was grown on 100-nm SiO_2/Si substrates via standard CVD growth procedures with MoO_3 and S precursors at 700 °C under continuous flow of N_2. See Supplementary Note 1 for a detailed description of the growth process and Supplementary Fig. 1 for optical and Raman characterization.

Near-field and confocal PL imaging. Scanning near-field PL imaging was performed on a customized NT-MDT scanning near-field optical microscope in a shear-force configuration as fully described in Supplementary Note 2. The Campanile tips were scanned over the sample at a distance of $\sim$5 nm. The excitation source was a linearly polarized 532-nm continuous wave laser. We estimate that 4 μW of excitation power were launched into the Campanile structure. The PL emission was collected by the same Campanile structure and analysed with a spectrometer with a cooled charge-coupled device camera. The far-field imaging of the PL was performed on the same NTMDT microscope in an upright confocal configuration with a $\times$100, 0.7-numerical aperture objective using the same 532-nm excitation source at 4.3 μW as measured at the back of the objective. The emission was collected and analysed by the same experimental setup as in the near-field measurements.

Campanile tip fabrication. The Campanile tip structures were fabricated at the end of an etched single-mode optical fibre as described in full detail in Supplementary Note 3. Scanning electron micrographs of the fabricated Campanile geometry are provided in Supplementary Fig. 3.

Nano-Auger microscopy. Nano-Auger electron spectroscopy was performed on an Oxford/Omnicron Nano-Auger system under ultra-high vacuum of 10^{-10} mbar. The size of the electron beam spot was $\sim$10 nm. The typical uncertainty in the nano-Auger composition measurement is $\sim$3%.

References

1. Mak, K. F., Lee, C., Hone, J., Shan, J. & Heinz, T. F. Atomically thin MoS_2: a new direct-gap semiconductor. *Phys. Rev. Lett.* **105,** 136805 (2010).
2. Splendiani, A. *et al.* Emerging photoluminescence in monolayer MoS_2. *Nano Lett.* **10,** 1271–1275 (2010).
3. Radisavljevic, B., Radenovic, A., Brivio, J., Giacometti, V. & Kis, A. Single-layer MoS_2 transistors. *Nat. Nanotechnol.* **6,** 147–150 (2011).
4. Wang, Q. H., Kalantar-Zadeh, K., Kis, A., Coleman, J. N. & Strano, M. S. Electronics and optoelectronics of two-dimensional transition metal dichalcogenides. *Nat. Nanotechnol.* **7,** 699–712 (2012).
5. Yin, Z. Y. *et al.* Single-Layer MoS_2 phototransistors. *ACS Nano* **6,** 74–80 (2012).
6. Ross, J. S. *et al.* Electrically tunable excitonic light-emitting diodes based on monolayer WSe_2 p-n junctions. *Nat. Nanotechnol.* **9,** 268–272 (2014).
7. Wu, W. *et al.* Piezoelectricity of single-atomic-layer MoS_2 for energy conversion and piezotronics. *Nature* **514,** 470–474 (2014).
8. Baugher, B. W. H., Churchill, H. O. H., Yang, Y. F. & Jarillo-Herrero, P. Optoelectronic devices based on electrically tunable p-n diodes in a monolayer dichalcogenide. *Nat. Nanotechnol.* **9,** 262–267 (2014).
9. Koppens, F. H. L. *et al.* Photodetectors based on graphene, other two-dimensional materials and hybrid systems. *Nat. Nanotechnol.* **9,** 780–793 (2014).
10. Fiori, G. *et al.* Electronics based on two-dimensional materials. *Nat. Nanotechnol.* **9,** 768–779 (2014).
11. Zhu, W. *et al.* Electronic transport and device prospects of monolayer molybdenum disulphide grown by chemical vapour deposition. *Nat. Commun.* **5,** 3087 (2014).
12. Ye, Z. L. *et al.* Probing excitonic dark states in single-layer tungsten disulphide. *Nature* **513,** 214–218 (2014).
13. Qiu, D. Y., da Jornada, F. H. & Louie, S. G. Optical spectrum of MoS_2: many-body effects and diversity of exciton states. *Phys. Rev. Lett.* **111,** 216805 (2013).
14. Chernikov, A. *et al.* Exciton binding energy and nonhydrogenic Rydberg series in monolayer WS_2. *Phys. Rev. Lett.* **113,** 076802 (2014).
15. Mak, K. F. *et al.* Tightly bound trions in monolayer MoS_2. *Nat. Mater.* **12,** 207–211 (2013).
16. Tongay, S. *et al.* Broad-range modulation of light emission in two-dimensional semiconductors by molecular physisorption gating. *Nano Lett.* **13,** 2831–2836 (2013).
17. Feng, J., Qian, X. F., Huang, C. W. & Li, J. Strain-engineered artificial atom as a broad-spectrum solar energy funnel. *Nat. Photonics* **6,** 865–871 (2012).
18. Liu, Z. *et al.* Strain and structure heterogeneity in MoS_2 atomic layers grown by chemical vapour deposition. *Nat. Commun.* **5,** 5246 (2014).
19. Van Der Zande, A. M. *et al.* Grains and grain boundaries in highly crystalline monolayer molybdenum disulphide. *Nat. Mater.* **12,** 554–561 (2013).
20. Helveg, S. *et al.* Atomic-scale structure of single-layer MoS_2 nanoclusters. *Phys. Rev. Lett.* **84,** 951–954 (2000).
21. Zhang, C., Johnson, A., Hsu, C. L., Li, L. J. & Shih, C. K. Direct imaging of band profile in single layer MoS_2 on graphite: quasiparticle energy gap, metallic edge states, and edge band bending. *Nano Lett.* **14,** 2443–2447 (2014).
22. Zhou, W. *et al.* Intrinsic structural defects in monolayer molybdenum disulfide. *Nano Lett.* **13,** 2615–2622 (2013).
23. Najmaei, S. *et al.* Vapour phase growth and grain boundary structure of molybdenum disulphide atomic layers. *Nat. Mater.* **12,** 754–759 (2013).
24. Chen, J. *et al.* Optical nano-imaging of gate-tunable graphene plasmons. *Nature* **487,** 77–81 (2012).
25. Fei, Z. *et al.* Gate-tuning of graphene plasmons revealed by infrared nano-imaging. *Nature* **487,** 82–85 (2012).
26. Fei, Z. *et al.* Electronic and plasmonic phenomena at graphene grain boundaries. *Nat. Nanotechnol.* **8,** 821–825 (2013).
27. De Angelis, F. *et al.* Nanoscale chemical mapping using three-dimensional adiabatic compression of surface plasmon polaritons. *Nat. Nanotechnol.* **5,** 67–72 (2010).
28. Bao, W. *et al.* Mapping local charge recombination heterogeneity by multidimensional nanospectroscopic imaging. *Science* **338,** 1317–1321 (2012).
29. Laquai, F., Park, Y. S., Kim, J. J. & Basche, T. Excitation energy transfer in organic materials: from fundamentals to optoelectronic devices. *Macromol. Rapid Commun.* **30,** 1203–1231 (2009).
30. Kagan, C. R., Murray, C. B., Nirmal, M. & Bawendi, M. G. Electronic energy transfer in CdSe quantum dot solids. *Phys. Rev. Lett.* **76,** 1517–1520 (1996).
31. Yin, X. B. *et al.* Edge nonlinear optics on a MoS_2 atomic monolayer. *Science* **344,** 488–490 (2014).
32. Huang, Y. L. *et al.* Bandgap tunability at single-layer molybdenum disulphide grain boundaries. *Nat. Commun.* **6,** 6298 (2015).
33. Xie, J. *et al.* Controllable disorder engineering in oxygen-incorporated MoS_2 ultrathin nanosheets for efficient hydrogen evolution. *J. Am. Chem. Soc.* **135,** 17881–17888 (2013).
34. Cui, X. *et al.* Multi-terminal transport measurements of MoS_2 using a van der Waals heterostructure device platform. *Nat. Nanotechnol.* **10,** 534–540 (2015).

Acknowledgements

We thank Ed Wong for technical support, as well as our colleagues at the Molecular Foundry for stimulating discussion and assistance. P.J.S. thanks Prof. L. Cao for insightful discussion and direction. Work at the Molecular Foundry was supported by the Director, Office of Science, Office of Basic Energy Sciences, Division of Materials Sciences and Engineering, of the U.S. Department of Energy under Contract No. DE-AC02-05CH11231. Material growth, preparation and nano-Auger characterization were supported by a NSF CAREER Award under Grant DMR-1055938.

Author contributions

W.B., N.J.B. and P.J.S. conceived the idea and initiated the project; S.T., W.F., J.S., C.K. and J.W. prepared the samples; W.B. fabricated the Campanile probes; W.B. and N.J.B.

conducted the near-field optical experiments; N.J.B. analysed the near-field optical data; C.K. and D.F.O. preformed nano-Auger mapping; A.T., S.A., Y.Z., A.B., P.D.A. and J.Z. performed and assisted sample characterization; N.J.B., W.B., and P.J.S. prepared the manuscript; P.J.S. and M.B.S. supervised the project; all authors contributed to discussions and manuscript revision.

Additional information

Supplementary Information accompanies this paper at http://www.nature.com/naturecommunications

Competing financial interests: The authors declare no competing financial interests.

Reprints and permission information is available online at http://npg.nature.com/reprintsandpermissions/

How to cite this article: Bao, W. *et al.* Visualizing nanoscale excitonic relaxation properties of disordered edges and grain boundaries in monolayer molybdenum disulfide. *Nat. Commun.* 6:7993 doi: 10.1038/ncomms8993 (2015).

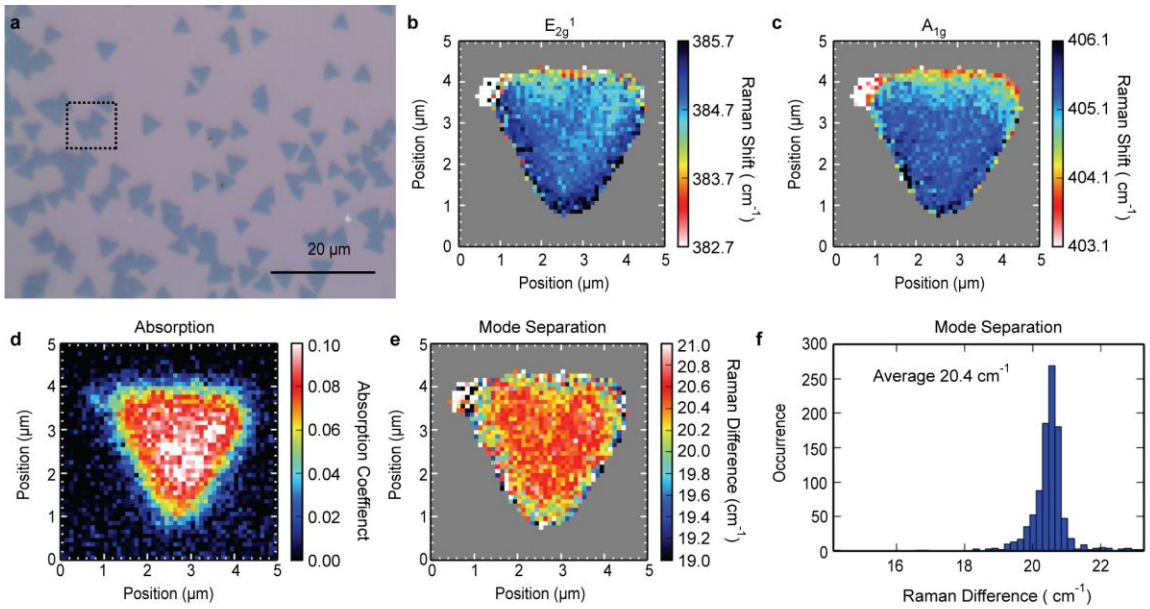

Supplementary Figure 1 – Optical characterization of the MoS_2 sample used in these measurements. **a.** Bright field optical microscopy of the monolayers of MoS_2 on the SiO_2/Si growth substrate. The black dashed line marks the flake that is shown in Fig. 4 of the main text. **b, c.** Spatial maps of energies of the E_{2g}^1 and A_{1g} modes measured using confocal Raman spectroscopy. **d.** Estimated MoS_2 absorption based on the relative attenuation of the Raman signal from the underlying Si substrate. **e, f.** The spatial and statistical distributions of the energetic splitting between the A_{1g} and E_{2g}^1 vibrational modes.

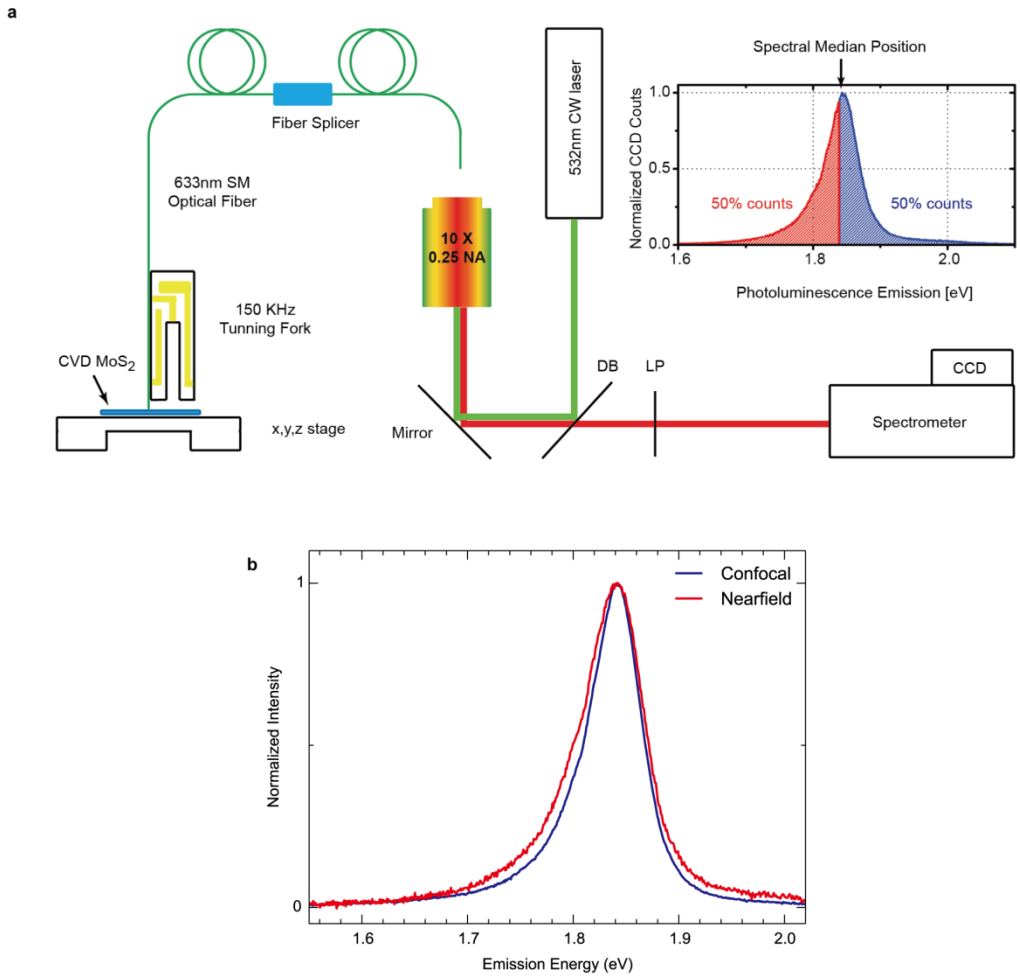

Supplmentary Figure 2 – Nearfield hyperspectral optical microscopy with the Campanile probe. **a.** Schematic drawing of our optical beam path. **b.** A comparison of the spatially averaged emission spectra collected from the Campanile nearfield probe and traditional confocal microscopy (100× 0.7 NA objective) for the ML-MoS_2 flake presented in Figure 1. For the nearfield measurement, the laser power before the fiber-slicer was 4 µW. The same excitation power was used for the confocal microscopy measurement as measured at the back aperture of the objective. The average emission spectra of the confocal and nearfield datasets are qualitatively similar, exhibiting emission from the exciton and trion states. We note that the width of the PL spectrum from the nearfield dataset is slightly broader and could be indicative of a larger excitation rate at the apex of the tip.

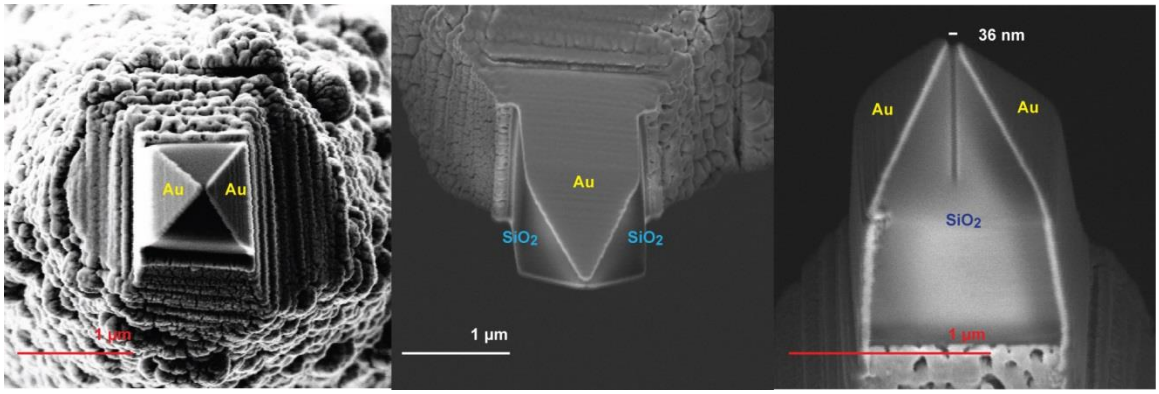

Supplementary Figure 3 – SEM images of a typical Campanile probe used in our measurement.

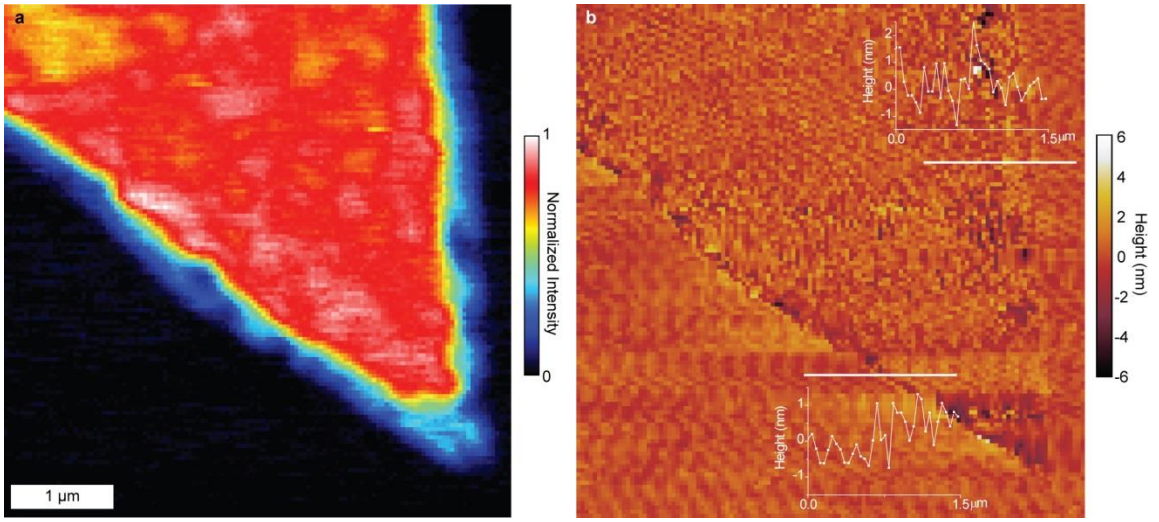

Supplementary Figure 4 – Comparison of a nano-PL map with the topography of a monolayer of MoS_2. **a.** A nano-PL map with nanoscale spatial variations. **b.** The measured topography from the shear-force feedback algorithm indicates that the monolayer of MoS_2 does not have topological features that correlate with the features seen in the PL. Two line cuts of its topography profile are also shown. The electronics of our shear-force microscope (NTMDT) typically exhibits a 0.5 nm noise in the height measurement. Since the physical size of the tip is larger than the nano-gap that determines the excitation volume, there is typically a 60 – 80 nm shift between the topography and optical datasets. The size of this shift is consistent with the thickness of the gold film on the Campanile probe.

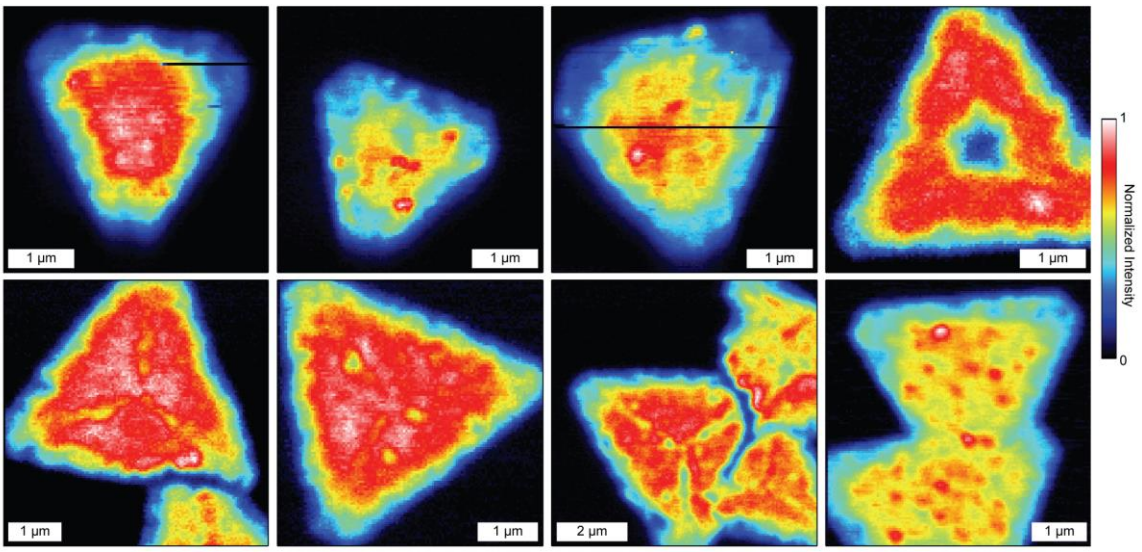

Supplementary Figure 5 – A collection of nano-PL maps from different monolayer MoS_2 flakes that were acquired during this study. All data were taken at the same excitation power as in the manuscript except for the upper-right panel where the excitation intensity was attenuated by a factor of 10.

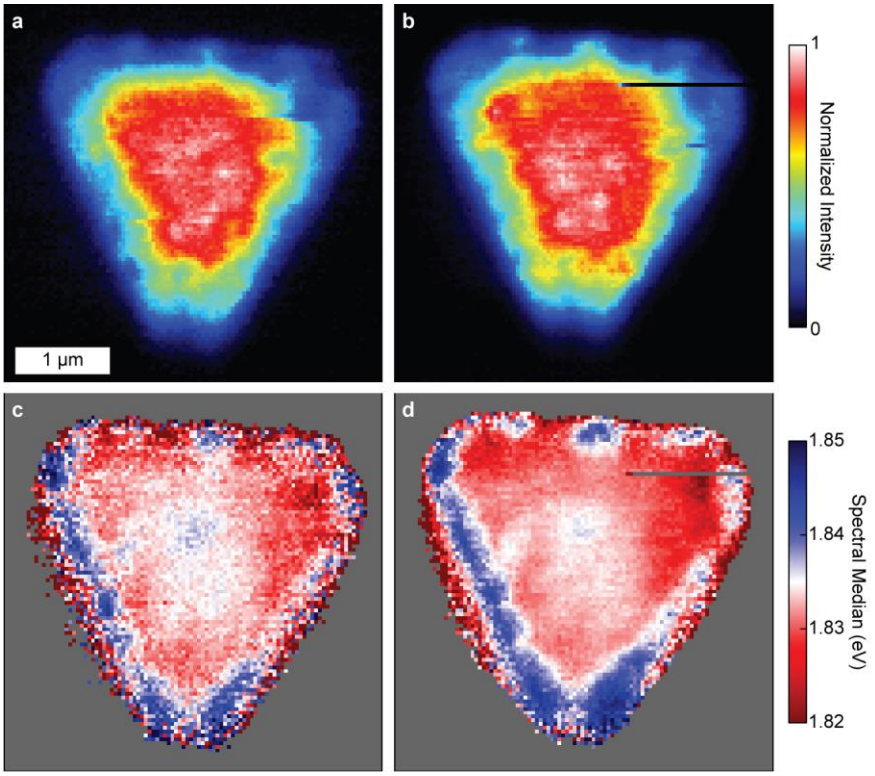

Supplementary Figure 6 – Nano-PL mapping of monolayer MoS_2 at two different excitation powers. Panels **a** and **b** show the PL intensity at ~0.27 μW and 2.7 μW, respectively. Features that are observed at lower excitation intensity are also observed at higher intensities with an improved signal to noise ratio. Correspondingly, the maps of the spectral median at the lower power (panel **c**) and higher power (panel **d**) exhibit the same features and numerical values indicating robustness over an order-of-magnitude in excitation intensity.

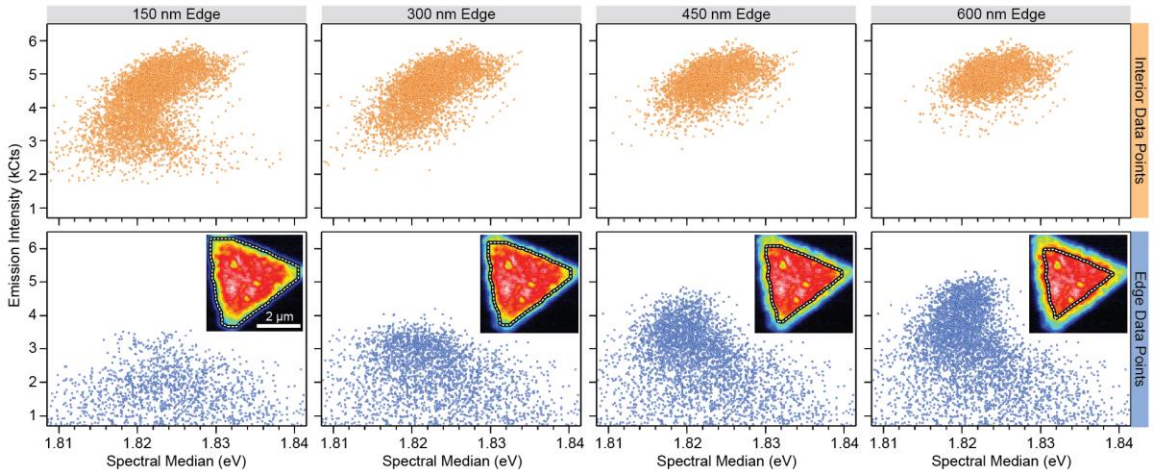

Supplementary Figure 7 – Emission intensity and spectral median correlation analysis for different edge widths. Each column in the above figure corresponds to the data analysis presented in Fig. 2c of the main text for a different edge width. The top row contains data points that are in the interior region of the flake, and edge points are in the bottom row. At an edge width of 150 nm (the first column), the correlation plot for the interior point exhibits two distinct features: a linear correlation and an uncorrelated band of points at low intensity. At edges widths of 450 nm and 600 nm (third and fourth column, respectively), two similar features emerges for the edge points. At an edge width of 300 nm (second column), the correlation plots for the interior and edges both exhibit a singular correlation.

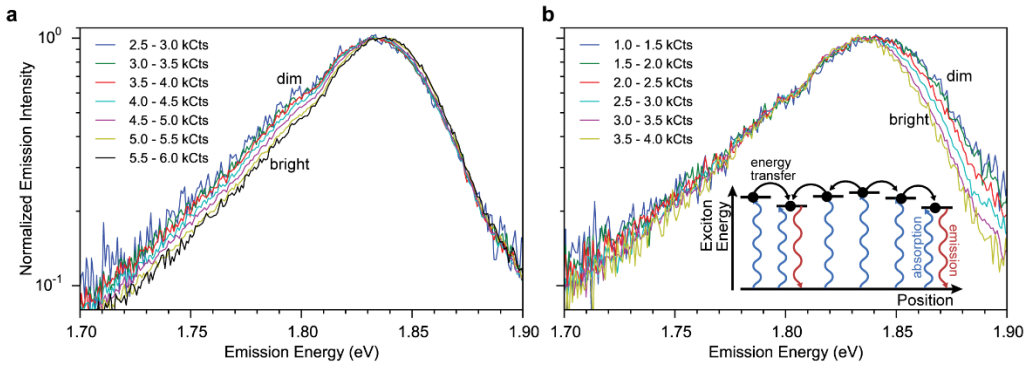

Supplementary Figure 8 – Average spectra of the PL of the ML-MoS_2 flake from Figure 2 grouped into finer ranges of intensity for the edge and interior regions. **a.** From the interior region, the average emission spectra of individual points grouped into seven equally spaced ranges of total intensity spanning 2.5 – 6.0 kCts confirms the trend in Fig. 2d where dimmer PL contains a larger relative amount of low-energy emission from the trion state. **b.** From the edge region, the average emission spectra of individual data points grouped into six evenly spaced bins spanning 1.0 - 4.0 kCts confirms the trend in Fig. 2e of the main text where dimmer PL exhibits increased broadening of the main exciton peak to higher energies. Inset: a schematic depiction of energetically disordered localized states. Efficient coupling between the states (i.e., energy transfer processes) can funnel excitation energy to the lowest energy sites which then dominate the PL process**.**

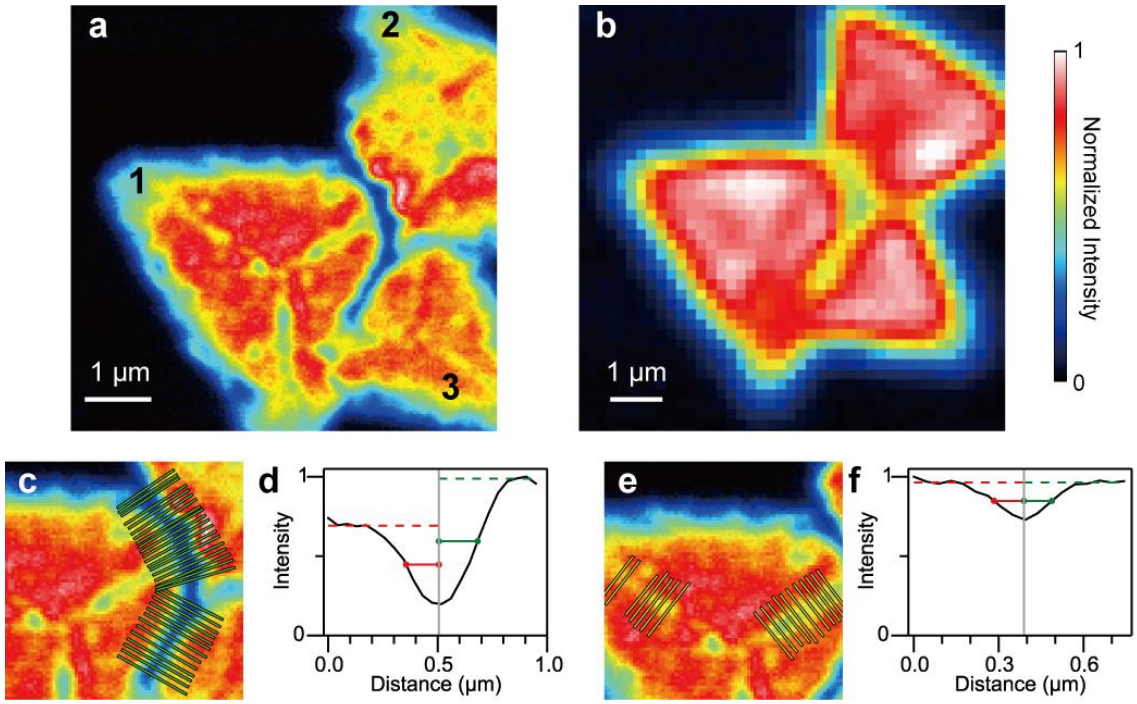

Supplementary Figure 9 – Excited state quenching at interflake and intraflake grain boundaries. **a.** PL intensity map of a multiflake aggregate of three ML-MoS_2 flakes (labeled 1, 2 and 3 in black lettering) forming three interflake grain boundaries. In the interior of flake 1, intraflake grain boundaries are observed extending from the center towards the apexes of the triangular flake. The interflake boundary quenches the PL intensity by 50-80%, whereas the intraflake boundary quenches the PL intensity by ~20%. **b.** An image of the same flakes acquired with a traditional scanning confocal microscope using a 100×, 0.7 NA objective. The significant nanoscale heterogeneity of the PL (panel a) is masked by the non-local excitation and collection of far-field confocal optics, and the PL quenching by the grain boundary is under estimated[6]. **c.** The positions of the line-sections (green markers) where the spatial extent of exciton quenching by the interflake grain boundaries presented in Figure 4 were measured. **d.** A sample line-section of the reduction in PL across the interflake grain boundary and the measurement of the asymmetric half-width-at-half-maximum (red and green lines) from the position that corresponds to the minimum emission intensity (gray line). **e,f.** The same plots as c and d for the intraflake grain boundaries.

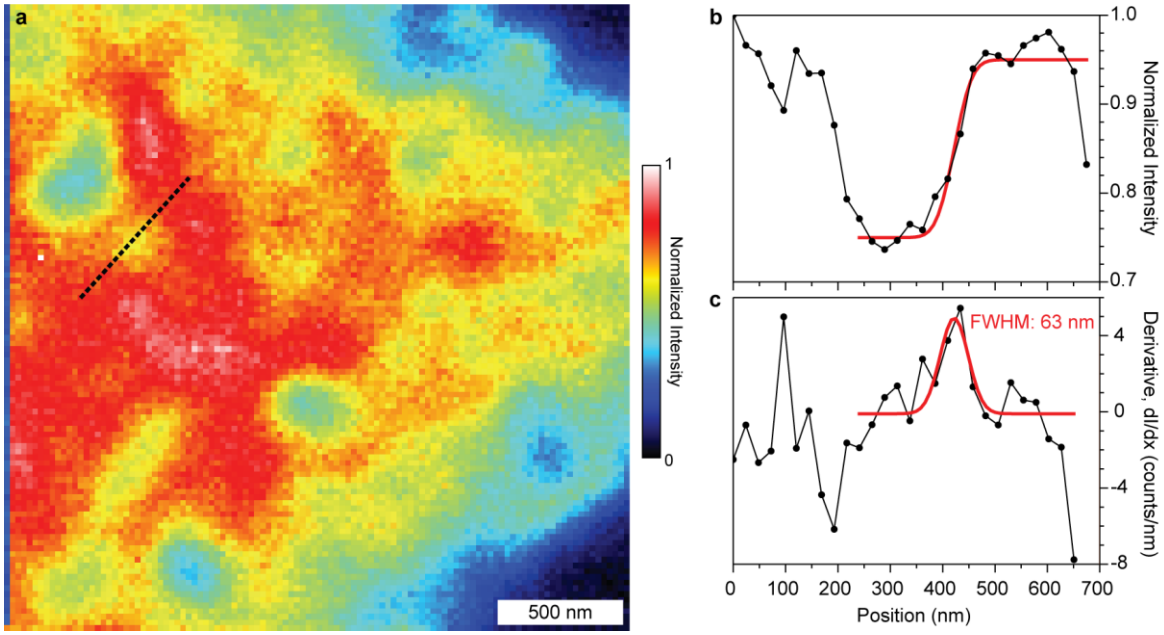

Supplementary Figure 10 – Estimate of spatial resolution. **a.** Map of the PL intensity of a monolayer of MoS_2. The dashed line marks a cross section where a sharp transition from dim to bright emission is observed. The intensity interpolated along this line is shown in panel **b** along with its spatial derivative in panel **c**, where the red lines in both panels show the Gaussian peak that was fitted to the derivative and then integrated to produce a step-like feature in the intensity plot.

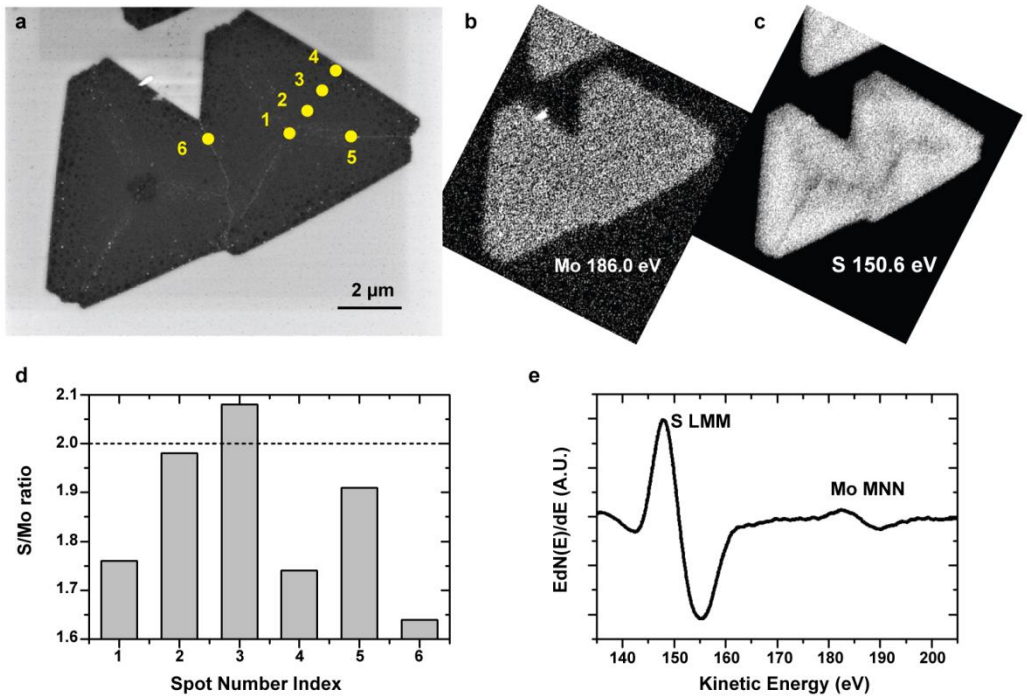

Supplementary Figure 11 – Scanning Auger Microscopy Characterization of MoS_2 flakes. **a.** SEM image of the MoS_2 flakes used in nano-Auger experiment. **b,c.** Elemental mapping of Mo (panel b) and S (panel c) based on Mo MNN (186.0 eV) and S LMM (150.6 eV) Auger transitions. Both the edge and grain boundaries are S-deficient while Mo composition is almost uniform over the CVD flakes. However, in the case of flakes with no clear boundary structures, chemical inhomogeneity is not observed. **d.** The stoichiometric S/Mo ratio at different location was determined by the peak-to-peak heights of primary S LMM and Mo MNN transitions obtained from the first derivative Auger spectra[8]. Boundaries (spot 5 and 6), edges (spot 4) and flake nucleation centers (spot 1) were confirmed to be S-deficient. The cleaved surfaces of bulk MoS_2 single crystals (supplied from 2D semiconductor and SPI) were used as references for chemical composition analysis. **e.** A typical Auger spectra of the MoS_2 showing both the Mo and S transition peaks.

Supplementary Note 1

CVD monolayer MoS_2 sample preparation and characterization

Monolayers of MoS_2 were grown on 100 nm SiO_2/Si substrates via CVD. Prior to growth, the substrates were cleaned in Piranha solution for 2 hours and then washed with deionized (DI) water. The substrates were placed face-down on the top of an alumina crucible that contained 3 mg of MoO_3 powder. A second crucible with S was placed upstream ~19 cm away from the MoO_3 source. The system was purged with ultrahigh purity N_2 gas at a flow rate of 500 sccm for 10 min and then heated to 300 °C over 10 min with the N_2 flowing at 100 sccm. The system was then heated to 700 °C within 15 min under 5 sccm of N_2 flow and then held at these conditions for 3 min. The furnace was then powered off. When the temperature reached 680 °C, the furnace was slightly opened by inserting a small metal part to prop open the top lid. At a temperature of 550 °C, the furnace was completely opened and the growth tube was fully removed from the furnace to achieve rapid cooling of the growth reaction. Sulfur boils at 450 °C and in our configuration, that S vapor was delivered to the growth region at a flow rate of ~2 sccm during the growth. During the cooling stage, S is continually supplied to the sample at flow rates ranging from 2-5 sccm to prevent sample degradation. The samples were characterized with Raman spectroscopy and show a <20.5 cm^{-1} separation between the A_{1g} and E^1_{2g} vibrational modes that is consistent with typical monolayer MoS_2 grown via CVD[1-3].

Supplementary Note 2

Experimental details of near-field imaging and spectroscopy

The near-field measurements were done on a customized NTMDT scanning nearfield optical microscope (NT-MDT NTEGRA Spectra) using a shear force head as shown in Supplementary Figure 2. An optical fiber that is terminated with the Campanile tip was glued to a tuning fork (2 mm × 6 mm; SCTF Electronics) with a resonance frequency of ~150 kHz. After attachment of the Campanile probe and in ambient conditions, a Q-factor of ~300 for the vibrational resonance was typically observed. The Campanile tip was kept ~5 nm above the sample during scanning, using the phase of the tuning fork oscillations for feedback (set point of 0.5°). Due to the temperature and pressure fluctuations in the lab, the tip was retracted 500 nm from the surface and re-approached after each line across the fast axis of the scan. While the tip was disengaged from the surface, the feedback loop was reset in order to account for temporal drift in the phase and maintain the stability of the tip-sample interaction over the full period of the measurement (2-8 hours). Linearly polarized excitation at 532 nm (Coherent Inc. Sapphire SF 532-100 CDRH) was spectrally filtered with a narrowband filter and coupled with an efficiency of 60% into the core of a patch single-mode optical fiber. At the exit of this patch fiber, the power of the excitation laser was ~4 μW. A mechanical fiber splicer (Thorlabs TS125) with a coupling efficiency about ~70% was used to connect the patch fiber to the fiber with the Campanile tip. Thus, we estimate that ~2.7 μW is launched into Campanile structure. The orientation of the polarization of the excitation light inside the fiber is controlled with an in-line Babinet–Soleil fiber polarization controller (Newport

Inc. F-POL-IL). The MoS_2 PL signal was collected with the same Campanile tip, optical fibers and coupling assembly. Two long-pass filters were used to filter the excitation light from the sample emission, which was then imaged onto a 200 μm circular entrance aperture of a spectrometer and ultimately detected with a cooled CCD camera (Andor iDus CCD DV401A-BV-600). For large area scans, hyperspectral maps were recorded with 200 ms integration time for each pixel, whereas the data in the smaller region (Fig. 3a) used a 10 s integration time.

The confocal μPL measurements were also performed with the same NT-MDT setup. A 100×, 0.7 NA objective was used to excite the sample at 532 nm and collect the resulting photoluminescence or Raman signal. The emission was analyzed through the same spectroscopy setup, employing a 50 μm pinhole.

Supplementary Note 3

Fabrication details for the Campanile probe

For a single Campanile tip, a Nufern S630-HP pure silica core single mode optical fiber (3.5 μm core diameter) was wet etched with 40% HF to shape a smooth cone with a half-cone-angle of ~18° and a tip-radius that is less than 200 nm. A 300 nm thick layer of a mixture of Pt and Au was sputtered on the fiber surface to ensure high conductivity in Ga^+ focused ion beam (FIB) milling (Zeiss Crossbeam 1540) process. The preliminary Campanile geometry was carved into the etched glass fiber tip by FIB milling. A subsequent 300 nm Pt/Au layer was deposited via sputtering to recoat the newly exposed SiO_2 surfaces with a conductive metal. A second FIB milling process was used to expose two opposing sides of the Campanile structure. Using tilt evaporation at 24°, a 3 nm Ti adhesion layer followed by a 70 nm thick Au layer and finally a 20 nm thick Cr protection layer were evaporated onto the structure on the SiO_2 surfaces that were exposed in the second FIB milling step to form the opposing metallic plates of the Campanile structure. After a final milling step to refine the shape and ensure that the metal plates are not connected, Cr etchant was used to strip the superfluous Cr layers, and finally a 2 nm thick layer of Al_2O_3 was deposited on the structure by atomic layer deposition at 40 °C. SEM micrographs of the final Campanile structures are shown in Supplementary Figure 3. Typically the resolution of the angle resolved evaporation was not sufficient to create a well-defined gap between the two triangular metallic plates at the apex. Thus, the gap was further cut using FIB milling, yielding gaps with dimensions that were typically 35-40 nm wide and 50 nm long (Supplementary Figure 3).

Supplementary Note 4

Intensity-spectrum correlation in the spatial variations of photoluminescence from monolayer MoS_2

In Figure 2c of the main text, it is shown that the spatial variations of the photoluminescence spectrum are correlated with variations in the integrated emission intensity. Further, the correlated behavior in the interior is distinct to that of a 300 nm wide peripheral edge region. To unravel the origins of the spectral fluctuations, we calculate the average emission spectra of sets of the individual hyperspectral data points that are grouped in ranges of increasing total emission intensity in Figures 2d and 2e for the interior and edge regions, respectively. We use the non-normalized spectrum (i.e., raw CCD counts) of each data point in the group to compute the average emission spectrum at the particular intensity level. This methodology enables the comparison of the typical emission spectrum of the dim regions of the MoS_2 flake to that of the bright regions. In Figs. 2d and 2e in the main text, we performed this analysis by dividing the data points into five intensity ranges that span an interval of 1000 counts (ranges I – V). In Supplementary Figure 8, the same analysis is repeated on the data from Figure 2 using smaller bin sizes (500 counts) to demonstrate that the identified trends are not artefacts of the choice of binning.

For the interior region (Figs. 2d and Supplementary Figure 8), the emission from dim regions of MoS_2 compared with that of the bright regions is found to have more relative low energy emission from the trion state with respect to the main exciton peak. In the edge region (Figure 2e and Supplementary Figure 8b), the behavior is markedly different.

Almost no variation is seen in the relative amount of trions in the PL, and the emission from the dim regions of the peripheral edge exhibits a high-energy broadening of the main exciton peak (an effect that is absent in the interior region). As discussed in the main text and depicted in the inset of Supplementary Figure 8b, such behavior is reminiscent of a disordered system that is comprised of an ensemble of localized states of different energies that are efficiently coupled, such as the chromophoric units of conjugated polymers[4] or individual quantum dots in a quantum dot solid[5]. Although all of states can be efficiently optically excited, efficient coupling between the states (i.e., energy transfer) rapidly depopulates the higher-energy states and funnels the excitation energy into the lowest energy sites which in turn dominate radiative relaxation (i.e., PL). This extra relaxation mechanism of the high-energy sites effectively reduces their PL quantum yield, thus reducing their brightness. Time-resolved spectroscopy combined with the nano-PL technique that is presented here could shed additional light on this relaxation mechanism. Because the higher-energy sites are predicted to have an additional, efficient non-radiative relaxation mechanism, their excited state lifetime should be substantially shorter than that of the lower-energy sites which lack this additional non-radiative relaxation pathway. Thus, spectrally and even possibly spatially resolved transient PL spectroscopy could provide significant insight into the optoelectronics of this peculiar edge region.

Supplementary Note 5

Estimate of spatial resolution

Without a single point emitter or discrete edge in the monolayer MoS_2, the spatial resolution can only be estimated from the sharpest observed features, which ranged from 50-80 nm. In Supplementary Figure 10, one such feature is extracted from the map of the PL intensity (Supplementary Figure 10a). Here, the feature corresponds to the transition from a dim area to a bright area (Supplementary Figure 10b), which can be analyzed using the knife-edge resolution test[7] to estimate our spatial resolution. Because the feature is a step function, its spatial derivative (Supplementary Figure 10c) is well-described by a Gaussian peak with a width that directly maps to the width of the transition region[7]. The full-width-at-half-maximum of the peak in the spatial derivative is 63 nm, corresponding to a 2σ width of 54 nm. In terms of a step (Supplementary Figure 10b), the 2σ width marks the extent of the transition from 15% to 84% of the step height, providing an estimate of our spatial resolution.

Supplementary References

1 Liu, K. *et al.* Elastic properties of chemical-vapor-deposited monolayer MoS_2, WS_2, and their bilayer heterostructures. *Nano Lett.* **14**, 5097-5103 (2014).

2 Najmaei, S. *et al.* Vapour phase growth and grain boundary structure of molybdenum disulphide atomic layers. *Nature Mater.* **12**, 754-759 (2013).

3 Liu, K. H. *et al.* Evolution of interlayer coupling in twisted molybdenum disulfide bilayers. *Nature Commun.* **5**, 4966 (2014).

4 Laquai, F., Park, Y. S., Kim, J. J. & Basche, T. Excitation Energy Transfer in Organic Materials: From Fundamentals to Optoelectronic Devices. *Macromol. Rapid Commun.* **30**, 1203-1231 (2009).

5 Kagan, C. R., Murray, C. B., Nirmal, M. & Bawendi, M. G. Electronic Energy Transfer in CdSe Quantum Dot Solids. *Phys. Rev. Lett.* **76**, 1517-1520 (1996).

6 van der Zande, A. M. *et al.* Grains and grain boundaries in highly crystalline monolayer molybdenum disulphide. *Nature Mater.* **12**, 554-561 (2013).

7 Levenson, E., Lerch, P. & Martin, M. C. Spatial resolution limits for synchrotron-based spectromicroscopy in the mid- and near-infrared. *Journal of Synchrotron Radiation* **15**, 323-328 (2008).

8 Childs, K. D. *et al.* Handbook of Auger electron spectroscopy. *Physical Electronics* (1995).